

## Roles of hydroxyl and oxygen vacancy of $\text{CeO}_2 \cdot x\text{H}_2\text{O}$ in Pd-catalyzed ethanol electro-oxidation

Zhenyu Li<sup>1,2</sup>, Jiefei Li<sup>1</sup>, Zexuan Zheng<sup>4</sup>, Kunhong Jiang<sup>1</sup>, Tianrun Zheng<sup>4</sup>, Dongmin Wang<sup>1</sup>, Hang Wei<sup>1</sup>, Zhiming Shi<sup>3\*</sup>, Xiaotian Li<sup>2\*</sup> & Haibin Chu<sup>1\*</sup>

<sup>1</sup>College of Chemistry and Chemical Engineering, Inner Mongolia Engineering and Technology Research Center for Catalytic Conversion and Utilization of Carbon Resource Molecules, Inner Mongolia University, Hohhot 010021, China;

<sup>2</sup>College of Materials Science and Engineering, Jilin University, Changchun 130022, China;

<sup>3</sup>State Key Laboratory of Luminescence and Applications, Changchun Institute of Optics, Fine Mechanics and Physics, Chinese Academy of Sciences, Changchun 130033, China;

<sup>4</sup>College of Chemistry, Jilin University, Changchun 130012, China

Received November 14, 2021; accepted March 2, 2022; published online April 15, 2022

In the field of noble metal-catalyzed alcohol electro-oxidation reaction (AOR), huge attention is paid on the composition, size, facet, and structure of the metals, while the support engineering should also be emphasized.  $\text{CeO}_2$  has been widely used as a unique support in AOR, primarily due to its abundant oxygen vacancies ( $\text{O}_v$ ). Herein, we report  $\text{CeO}_2 \cdot x\text{H}_2\text{O}$  nanoparticles with both massive hydroxyl groups (OH) and  $\text{O}_v$  remarkably enhance the catalytic activity and stability of Pd toward ethanol oxidation reaction (EOR). The CO stripping experiments and density functional theory (DFT) calculations suggest that OH and  $\text{O}_v$  on  $\text{CeO}_2 \cdot x\text{H}_2\text{O}$  surface bring about a large downshift of Pd d-band center and a significant weakening of CO adsorption on Pd. Moreover, OH and  $\text{O}_v$  also play synergic roles in the removal of toxic intermediates. Consequently, the important roles of OH and  $\text{O}_v$  of  $\text{CeO}_2 \cdot x\text{H}_2\text{O}$  are confirmed in Pd-catalyzed EOR. The facile  $\text{CeO}_2 \cdot x\text{H}_2\text{O}$ -enhanced strategy can contribute to the catalyst design for other energy conversion reactions.

**electrocatalysis, ceria, hydroxyl, oxygen vacancy, ethanol oxidation reaction**

**Citation:** Li Z, Li J, Zheng Z, Jiang K, Zheng T, Wang D, Wei H, Shi Z, Li X, Chu H. Roles of hydroxyl and oxygen vacancy of  $\text{CeO}_2 \cdot x\text{H}_2\text{O}$  in Pd-catalyzed ethanol electro-oxidation. *Sci China Chem*, 2022, 65: 877–884, <https://doi.org/10.1007/s11426-021-1220-2>

### 1 Introduction

The ethanol oxidation reaction (EOR) is a crucial half-reaction in direct ethanol fuel cells (DEFCs) [1–3]. Over the past several decades, Pd is found to be the most promising catalyst for EOR in alkaline medium because of its unique electronic structure and oxophilicity [4–7]. However, the development of a highly active and stable Pd-based electrocatalyst is of significant challenge, as often impeded by the adsorption of CO, which deactivates the catalyst during

EOR [8,9]. To address this problem, the strategies including alloying, introduction of metal oxides (*e.g.*,  $\text{CeO}_2$ ,  $\text{SnO}_2$ ,  $\text{WO}_3$ , and  $\text{MnO}_2$ ) and hydroxides (*e.g.*,  $\text{Ni}(\text{OH})_2$  and  $\text{Co}(\text{OH})_2$ ) are found to be effective [4,10–16]. The surface of metal oxides or hydroxides affords much reactive OH, which is essential for the removal of the important intermediates  $\text{CO}_{\text{ads}}$  and  $\text{CH}_{\text{ads}}$  on Pd during EOR [15,17–22]. Thus, the high content of OH is conducive to the catalytic performance toward EOR.

Among the metal oxides,  $\text{CeO}_2$  has attracted unique attention in alcohol electro-oxidation reactions, primarily arising from two aspects. First, the strong metal-support interaction between Pd and  $\text{CeO}_2$  mediates the adsorption of

\*Corresponding authors (email: [chuhb@imu.edu.cn](mailto:chuhb@imu.edu.cn); [shizm@ciomp.ac.cn](mailto:shizm@ciomp.ac.cn); [xiaotianli@jlu.edu.cn](mailto:xiaotianli@jlu.edu.cn))

ethanol and the reaction intermediates on the catalyst surface [23,24]. Second, the oxygen vacancies ( $O_v$ ) on  $CeO_2$  surface afford reactive  $OH_{ads}$  via water dissociation, accelerating the oxidation of  $CO_{ads}$  and  $CH_{ads}$  on Pd [25,26]. Apart from  $O_v$ , we recently revealed that the intrinsic OH groups on  $CeO_2$  can also enhance the catalytic activity and stability of Pt/CNT toward alcohol oxidation reaction [27]. However, it remains unclear whether  $O_v$  and OH can synergically enhance the catalytic performance of the metal catalysts. Meanwhile, the enhancement mechanism of  $O_v$  and OH is not well understood. Herein, we design four types of  $CeO_2$  (Scheme 1),  $CeO_2$  with few OH and  $O_v$  (denoted as  $CeO_2$ ),  $CeO_2$  with abundant OH but few  $O_v$  ( $CeO_2$ -OH),  $CeO_2$  with abundant  $O_v$  but few OH ( $CeO_2$ - $O_v$ ), and  $CeO_2$  with plenty of both OH and  $O_v$  ( $CeO_2 \cdot xH_2O$ ). These  $CeO_2$  particles are directly loaded with Pd nanoparticles, without any carbon support, to unveil the respective effect of OH and  $O_v$ . Both experimental and theoretical investigations reveal that OH and  $O_v$  not only individually enhance the catalytic performance of Pd, but also play the synergic roles. The OH can stabilize the  $O_v$  on  $CeO_2$ , and further improve the ability toward  $CO_{ads}$  removal, leading to the high EOR performance.

## 2 Experimental

### 2.1 Chemicals and reagents

$CeCl_3 \cdot 7H_2O$ , *tert*-butylamine, ethylene glycol (EG), and  $NaBH_4$  were purchased from Sinopharm Chemical Reagent Co., Ltd.  $Pd(NO_3)_2$  was obtained from Aladdin Chemistry Co., Ltd. Ethanol and KOH were purchased from Beijing Chemical Factory. The Nafion perfluorinated resin solution and L-lysine were bought from Alfa Aesar. The commercial catalysts of Pt/C, PtRu/C, and Pd/C were bought from Johnson Matthey. Highly purified water ( $>18 M\Omega$  cm resistivity) was provided by a PALL PURELAB Plus system.

### 2.2 Material preparation

#### 2.2.1 Synthesis of $CeO_2 \cdot xH_2O$ nanoparticles

$CeCl_3 \cdot 7H_2O$  (0.1480 g) was dissolved into the mixed solvents of 9.0 mL EG and 1.0 mL deionized water, which was then stirred for 10 min. Subsequently, 6 mL of *tert*-butyla-

mine was dropped into the above solution under continuous stirring for 90 min. The yellow solution was transferred into a Teflon-lined autoclave, which was then heated from room temperature to 180 °C for 8 h. Finally, the yellow precipitate was centrifuged, washed several times with deionized water and ethanol, and dried at 80 °C to achieve  $CeO_2 \cdot xH_2O$  nanoparticles.

#### 2.2.2 Preparation of $CeO_2$ nanoparticles

The  $CeO_2 \cdot xH_2O$  nanoparticles were placed in a crucible, which was then heated from room temperature to 400 °C in a muffle furnace at a rate of 4 °C  $min^{-1}$ , and kept for 2 h to get  $CeO_2$  nanoparticles.

#### 2.2.3 Preparation of $CeO_2$ - $O_v$ nanoparticles

$CeO_2$ - $O_v$  was prepared according to a modified approach in previous report [28]. The 50 mg of the as-prepared  $CeO_2$  nanoparticles was dispersed in the mixed solution of 20 mL of 1 M NaOH and 20 mL of EG, which was transferred into a Teflon-lined autoclave. The autoclave was heated at 140 °C for 12 h. The precipitate was washed with ethanol and water for three times, respectively, and dried at 80 °C to obtain  $CeO_2$ - $O_v$  nanoparticles.

#### 2.2.4 Preparation of $CeO_2$ -OH nanoparticles

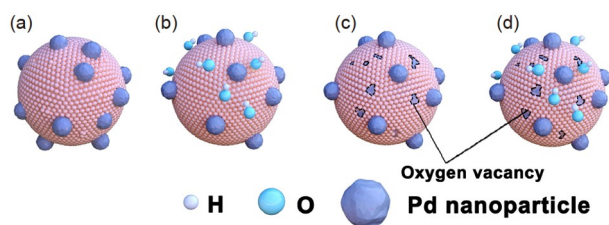
The 50 mg of the as-prepared  $CeO_2$  nanoparticles was dispersed in 20 mL of 1.0 M NaOH solution in a 100 mL round-bottomed flask, which was then stirred for 24 h. The precipitate was washed with ethanol and water for three times, respectively, and dried at 80 °C to obtain  $CeO_2$ -OH nanoparticles.

#### 2.2.5 Preparation of $Pd/CeO_2 \cdot xH_2O$ , $Pd/CeO_2$ - $O_v$ , $Pd/CeO_2$ -OH, and $Pd/CeO_2$

The  $CeO_2 \cdot xH_2O$  nanoparticles and L-lysine were added into 20 mL of water to form the mixture, which was centrifuged at 8,000 r/min to get the precipitate. The above procedure was repeated for three times, after which 60 mg of the L-lysine-modified  $CeO_2 \cdot xH_2O$  was redistributed into water with vigorous stirring to form an uniform mixture in the ice-cooled water bath. Afterwards, 4 mL of  $Pd(NO_3)_2$  solution (0.0937 mmol/mL) was transferred into the above mixture, after which the mixture was stirred for another 10 min. Then, 50 mg of  $NaBH_4$  (dissolved in 5 mL water) was injected into the above mixture dropwise, and the mixture was kept stirring for 1 h. The product of  $Pd/CeO_2 \cdot xH_2O$  was obtained by treated with water and ethanol for several times to remove L-lysine, and finally dried at 60 °C for 8 h. The  $Pd/CeO_2$ - $O_v$ ,  $Pd/CeO_2$ -OH, and  $Pd/CeO_2$  were prepared via the same procedure except for the different  $CeO_2$  support.

### 2.3 Material characterizations

The powder X-ray diffraction (XRD) patterns of the mate-



**Scheme 1** The models of  $Pd/CeO_2$  (a),  $Pd/CeO_2$ -OH (b),  $Pd/CeO_2$ - $O_v$  (c), and  $Pd/CeO_2 \cdot xH_2O$  (d) (color online).

rials were obtained on X-ray diffractometer (Rigaku D/Max 2550) using Cu K $\alpha$  radiation ( $\lambda = 1.5418 \text{ \AA}$ ). The transmission electron microscope (TEM) and high-resolution TEM (HRTEM) images were recorded by a Philips-FEI Tecnai G2STwin microscope equipped with a field emission gun operating at 200 kV. X-ray photoelectron spectroscopy (XPS) spectra were collected using a Thermo Fisher Scientific ESCALAB 250Xi with photoelectron spectroscopy system using a monochromatic Al K $\alpha$  (1486.6 eV) X-ray source. Electron paramagnetic resonance (EPR) signals were obtained on an X-band JES FA-200 EPR spectrometer at room temperature. The Raman spectra of the materials were recorded on a Renishaw Raman system model 1000 spectrometer operating with an air-cooled argon ion laser (532 nm, 20 mW) as the excitation light source. Thermogravimetric analysis (TGA) was performed using a Netzsch STA 409PC instrument in the range of 25–800 °C at a heating speed of 5 °C/min. The determination of Pd-d-band center position was achieved by the high-resolution ultraviolet photoelectron spectroscopy (UPS) measurements by using He II ( $h\nu = 21.22 \text{ eV}$ ) ultraviolet excitation lines excited with a vacuum generators (VG) He discharge source, and a negative bias voltage of 15 V was applied to all the samples to accelerate electrons of low kinetic energy and therefore to allow for an accurate determination of the secondary electron cutoff. The valence band photoemission spectra were obtained after subtraction of the background and integration over the valence band region.

## 2.4 Electrochemical measurements

All electrochemical tests were conducted with a CHI 760E electrochemical workstation. The glassy carbon electrode (GCE) with a diameter of 3 mm, saturated calomel electrode (SCE), and Pt wire were used as the working electrode, reference electrode, and counter electrode, respectively. To prepare the ink of catalyst, 2.5 mg of Pd/CeO $_2 \cdot x\text{H}_2\text{O}$  catalyst, 300  $\mu\text{L}$  of water, 1,180  $\mu\text{L}$  of ethanol, and 20  $\mu\text{L}$  of conductive polymer binder (0.3% Nafion solution) were mixed and ultrasonicated for 30 min to form the uniform ink. Then, 5  $\mu\text{L}$  of the ink was dropped onto the GCE and then dried naturally. The loading amount of Pd was 3.3 mg on the surface of GCE.

Cyclic voltammograms (CVs) measurements were conducted in a N $_2$ -saturated 1.0 M KOH and 1.0 M CH $_3$ CH $_2$ OH solution within the potential range of  $-0.9$  to  $0.2 \text{ V}$  at the scan rate of  $50 \text{ mV/s}$ . The current-time curves were recorded in 1.0 M KOH +1.0 M CH $_3$ CH $_2$ OH at  $-0.3 \text{ V}$ . The polarization curve tests were conducted in the range of  $-0.9$  and  $0.4 \text{ V}$  with a scan rate of  $1 \text{ mV/s}$ . The CO stripping tests were conducted between  $-0.9$  and  $0.2 \text{ V}$  in a CO-saturated 1.0 M KOH solution. Electrochemical impedance spectra (EIS) were carried out in a frequency range from 1 to 100,000 Hz

with an AC voltage amplitude of 5.0 mV. For comparative purpose, the catalytic activities of the commercial Pt/C, Pd/C, and PtRu/C with the same noble metal loading were evaluated under the same conditions.

## 2.5 Theoretical calculations

### 2.5.1 Computations of CO adsorption free-energy and electronic structure

All the density functional theory (DFT) calculations were carried out using the Vienna *ab initio* simulation package (VASP), and the plane wave basis set was employed. The highly localized Ce 4f-orbitals were precisely treated by using spin-polarized DFT +  $U$  calculations, and a value of  $U_{\text{eff}} = 5.0 \text{ eV}$  was applied to the Ce 4f state. The previous studies have verified the  $U$  value of 5 eV could precisely describe the electronic structure of the reduced ceria. The projector-augmented wave (PAW) method was used to represent the core-valence interaction. During the calculative process, the generalized gradient approximation (GGA) was used in the form of revised Perdew-Burke-Ernzerhof (RPBE) with Pade Approximation and the plane wave energy cutoff was set to 400 eV. To speed up the convergence of electronic structure optimization, the Gaussian smearing method with the width of 0.05 eV was used. The Brillouin zone was sampled at the  $\Gamma$ -point. The convergence criteria for the energy and force were set to  $10^{-5} \text{ eV}$  and  $0.02 \text{ eV/\AA}$ , respectively. The adsorption free energy of CO ( $\Delta G_{\text{CO}^*}$ ) was calculated by the Eq. (1) [29]:

$$\Delta G_{\text{CO}^*} = E_{\text{CO}^*} - E_{\text{metal surface}} - E_{\text{CO}} \quad (1)$$

where  $E_{\text{CO}^*}$ ,  $E_{\text{CO}}$ , and  $E_{\text{metal surface}}$  represent the total energy of the interacting adsorbate and metal surface system, energies of the free adsorbate in gas phase, and bare metal surface, respectively.

According to d-band model, d-band center is the simplest descriptor to describe the adsorption energy of adsorbate. And it can be defined by Eq. (2) [30]:

$$\varepsilon_d = \frac{\int_{-\infty}^{\infty} n_d(\varepsilon)\varepsilon d\varepsilon}{n_d(\varepsilon)d\varepsilon} \quad (2)$$

where  $\varepsilon$  is the energy referring to E-Fermi, and  $n_d(\varepsilon)$  is the density of states projected onto d-states.

### 2.5.2 Computational models

The CeO $_2$  (111) surface is the most stable among the common facets exposed at ceria oxide according to previous work [31]. Accordingly, we constructed a slab model of CeO $_2$  (111) surface with 9 atomic layers. The surface supercell was set to  $3 \times 3$  and the model contains total 81 atoms. To minimize the atomic interaction, we set a vacuum gap with 12  $\text{\AA}$ . The atoms in the bottom three atomic layers were fixed in the bulk position during geometry optimization.

tion, while the rest of the other atom layers and Pd cluster were relaxed. The  $\text{CeO}_2\text{-OH}$  (111) and  $\text{CeO}_2\text{-O}_v$  (111) models were constructed by adding a hydroxyl group and removing an oxygen atom on the top surface of the  $\text{CeO}_2$  (111) surface, respectively [31,32]. The  $\text{CeO}_2\cdot x\text{H}_2\text{O}$  (111) model was constructed by adding a hydroxyl group, while removing an oxygen atom on the top surface of the  $\text{CeO}_2$  (111) surface [33,34]. Pd/ $\text{CeO}_2\text{-O}_v$ , Pd/ $\text{CeO}_2\text{-OH}$ , Pd/ $\text{CeO}_2$ , and Pd/ $\text{CeO}_2\cdot x\text{H}_2\text{O}$  systems were modeled by adding Pd cluster with six atoms on the surface of  $\text{CeO}_2$  (111),  $\text{CeO}_2\text{-OH}$  (111),  $\text{CeO}_2\text{-O}_v$  (111), and  $\text{CeO}_2\cdot x\text{H}_2\text{O}$  (111), respectively. In order to get the most stable structure of  $\text{CeO}_2$ -supported Pd nanoparticle, the molecular dynamic simulations were carried out at 300 K before we calculated the structures and the adsorption energy. We selected four optimized and the most stable structures to calculate the adsorption free energy of CO on *fcc* site of Pd cluster.

### 3 Results and discussion

#### 3.1 Characterizations of hydroxyl and oxygen vacancy on the four types of $\text{CeO}_2$

We synthesized the  $\text{CeO}_2\cdot x\text{H}_2\text{O}$  nanoparticles by solvothermal method, in which  $\text{CeCl}_3\cdot 7\text{H}_2\text{O}$  was used as the cerium precursor in ethylene glycol and water, and *tert*-butylamine was explored as protection agent and  $\text{OH}^-$  precursor. Transmission electron microscopy (TEM) image of  $\text{CeO}_2\cdot x\text{H}_2\text{O}$  nanoparticles reveals they have the uniform size of  $10.9 \pm 2.2$  nm (Figure S1a, Supporting Information online). After calcined at 400 °C for 2 h,  $\text{CeO}_2\cdot x\text{H}_2\text{O}$  nanoparticles were transformed into  $\text{CeO}_2$  nanoparticles with reduced content of OH and  $\text{O}_v$ . To increase the OH content,  $\text{CeO}_2$  nanoparticles were stirred in NaOH solution for 24 h to get  $\text{CeO}_2\text{-OH}$ . To increase the  $\text{O}_v$  concentration,  $\text{CeO}_2$  nanoparticles were solvothermally treated in the mixture solution of NaOH and ethylene glycol at 140 °C for 12 h to obtain  $\text{CeO}_2\text{-O}_v$ . TEM images exhibit that  $\text{CeO}_2$ ,  $\text{CeO}_2\text{-O}_v$ , and  $\text{CeO}_2\text{-OH}$  particles possess the slightly increased sizes of  $14.0 \pm 3.3$  nm,  $13.7 \pm 3.1$  nm, and  $13.5 \pm 2.7$  nm, respectively (Figure S1). High-resolution TEM images show all the four samples have the typical (111) plane of  $\text{CeO}_2$  (Figure S2). X-ray diffraction (XRD) patterns exhibit they all have a cubic fluorite structure of  $\text{CeO}_2$  (Figure S3). Unlike those of  $\text{CeO}_2\text{-O}_v$ ,  $\text{CeO}_2\text{-OH}$ , and  $\text{CeO}_2$ , the peaks of  $\text{CeO}_2\cdot x\text{H}_2\text{O}$  are relatively weak, suggesting the low crystallinity of the sample.

We quantitatively analyze the content of hydroxyl in the  $\text{CeO}_2\cdot x\text{H}_2\text{O}$ ,  $\text{CeO}_2\text{-OH}$ ,  $\text{CeO}_2\text{-O}_v$ , and  $\text{CeO}_2$  using TGA. The TGA curves present two stages of weight loss (Figure 1a). The weight loss from 25 to 200 °C is ascribed to the free water in the samples, and the weight loss from 200 to 600 °C is due to the partial dehydration of  $\text{Ce}(\text{OH})_4$  into  $\text{CeO}_2$  [35].

The latter losses for  $\text{CeO}_2\cdot x\text{H}_2\text{O}$ ,  $\text{CeO}_2\text{-OH}$ ,  $\text{CeO}_2\text{-O}_v$ , and  $\text{CeO}_2$  are 8.8%, 4.8%, 4.4%, and 2.0% (Figure S4), respectively. Accordingly, the hydroxyl contents in the samples are 16.6%, 9.1%, 8.2%, and 3.7%, respectively [35]. The XPS spectra of O 1s further illustrate the presence of OH groups at 530.3 eV (Figure 1b) [36]. The content of surface OH groups also decreases in the order of  $\text{CeO}_2\cdot x\text{H}_2\text{O}$ ,  $\text{CeO}_2\text{-OH}$ ,  $\text{CeO}_2\text{-O}_v$ , and  $\text{CeO}_2$ . Moreover, the absorption bands around  $3410\text{ cm}^{-1}$  in the infrared spectra of  $\text{CeO}_2\cdot x\text{H}_2\text{O}$ ,  $\text{CeO}_2\text{-OH}$ , and  $\text{CeO}_2\text{-O}_v$  are much stronger than that of  $\text{CeO}_2$ , again verifying more OH groups on their surface (Figure S5) [37].

To compare the oxygen vacancy content in  $\text{CeO}_2\cdot x\text{H}_2\text{O}$ ,  $\text{CeO}_2\text{-O}_v$ ,  $\text{CeO}_2\text{-OH}$ , and  $\text{CeO}_2$  nanoparticles, X-ray photoelectron spectroscopy (XPS), Raman spectroscopy, and X-band EPR spectroscopy were explored. As shown in Figure 1c, the deconvoluted peaks at 880.5, 884.4, 898.8, and 903.2 eV are attributed to  $\text{Ce}^{3+}$ , while other six peaks are assigned to  $\text{Ce}^{4+}$  [38]. Both  $\text{CeO}_2$  and  $\text{CeO}_2\text{-OH}$  exhibit low  $\text{Ce}^{3+}$  fractions of 15.1% and 15.7%. In contrast,  $\text{Ce}^{3+}$  fractions in  $\text{CeO}_2\text{-O}_v$  and  $\text{CeO}_2\cdot x\text{H}_2\text{O}$  increase to 25.6% and 33.6%, respectively, suggesting their higher content of  $\text{O}_v$ . The Raman spectra (Figure S6) also suggest  $\text{CeO}_2\cdot x\text{H}_2\text{O}$  possesses the highest  $\text{O}_v$  concentration among the four samples, by comparing the relative intensity of peaks at 598 and  $461\text{ cm}^{-1}$  [39]. Figure 1d shows EPR spectra of the samples, and the signal of  $g = 1.96$  reflects the  $\text{O}_v$  on the particle surface [40]. The strong peaks appear on  $\text{CeO}_2\text{-O}_v$  and  $\text{CeO}_2\cdot x\text{H}_2\text{O}$ , while rather weak signals are observed on  $\text{CeO}_2$  and  $\text{CeO}_2\text{-OH}$ . All the results confirm that the  $\text{O}_v$  content decreases in the order of  $\text{CeO}_2\cdot x\text{H}_2\text{O} > \text{CeO}_2\text{-O}_v > \text{CeO}_2\text{-OH} > \text{CeO}_2$ .

#### 3.2 Ethanol electro-oxidation performance on the four catalysts

Then,  $\text{CeO}_2\cdot x\text{H}_2\text{O}$ ,  $\text{CeO}_2\text{-O}_v$ ,  $\text{CeO}_2\text{-OH}$ , and  $\text{CeO}_2$  nanoparticles are used to load ~40 wt% Pd nanoparticles *via* a facile  $\text{NaBH}_4$  reduction method, using L-lysine as the linkage (Figure 2a). XRD patterns, low- and high-resolution TEM images (Figure 2b–d and Figure S7) reveal the formation of Pd/ $\text{CeO}_2\cdot x\text{H}_2\text{O}$ , Pd/ $\text{CeO}_2\text{-O}_v$ , Pd/ $\text{CeO}_2\text{-OH}$ , and Pd/ $\text{CeO}_2$  composites with the close size of Pd particles 4.8, 5.3, 5.3, and 4.4 nm, respectively. Element mappings of Pd/ $\text{CeO}_2\cdot x\text{H}_2\text{O}$  indicate the uniform distribution of Pd nanoparticles on  $\text{CeO}_2\cdot x\text{H}_2\text{O}$  (Figure 2e and f). Meanwhile,  $\text{CeO}_2\cdot x\text{H}_2\text{O}$  retains its original OH and  $\text{O}_v$  after Pd loading, and possesses a significant higher content of OH and  $\text{O}_v$  than those in Pd/ $\text{CeO}_2\text{-O}_v$ , Pd/ $\text{CeO}_2\text{-OH}$ , and Pd/ $\text{CeO}_2$ , as revealed by XPS and EPR results (Figures S8 and S9).

Next, we use EOR as the model reaction to investigate the effect of OH and  $\text{O}_v$  on the electrocatalytic performance of the four catalysts. The EOR activities were evaluated in the mixed solution of 1.0 M KOH and 1.0 M  $\text{CH}_3\text{CH}_2\text{OH}$ . As

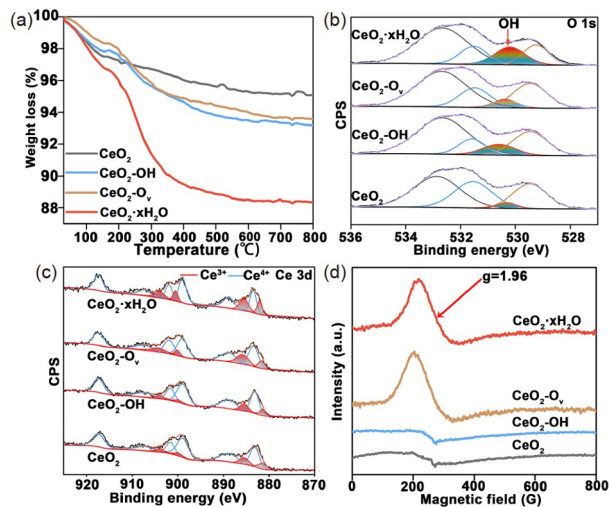


**Figure 1** TGA curves (a), O 1s XPS spectra (b), Ce 3d XPS spectra (c), and X-band EPR spectra (d) of CeO<sub>2</sub>, CeO<sub>2</sub>-OH, CeO<sub>2</sub>-O<sub>v</sub>, and CeO<sub>2</sub>·xH<sub>2</sub>O (color online).

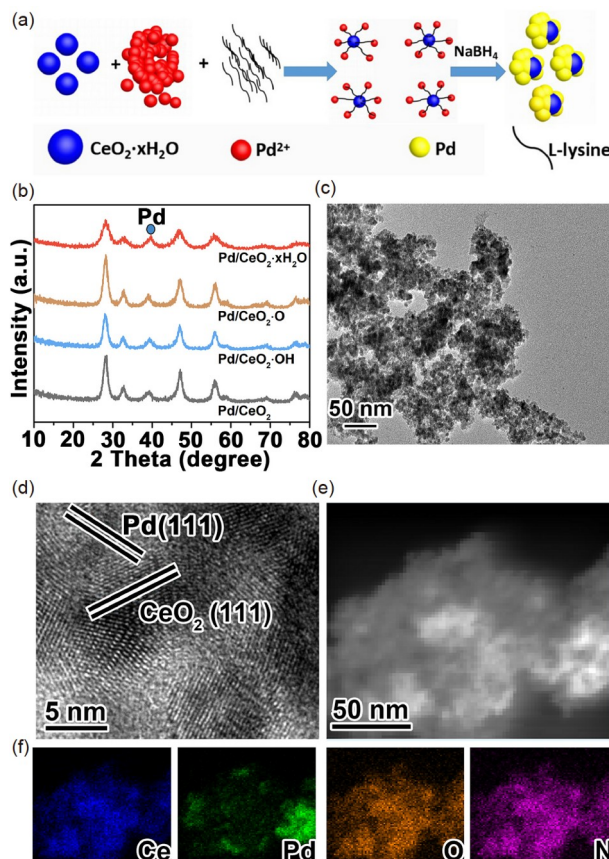


**Figure 2** (a) The synthesis procedure of the Pd/CeO<sub>2</sub>·xH<sub>2</sub>O catalyst; (b) XRD patterns of Pd/CeO<sub>2</sub>, Pd/CeO<sub>2</sub>-OH, Pd/CeO<sub>2</sub>-O<sub>v</sub>, and Pd/CeO<sub>2</sub>·xH<sub>2</sub>O; (c) TEM, and (d) HRTEM images of Pd/CeO<sub>2</sub>·xH<sub>2</sub>O; (e) STEM image and (f) the corresponding element mappings of Pd/CeO<sub>2</sub>·xH<sub>2</sub>O (color online).

shown in Figure 3a and Table 1, the Pd/CeO<sub>2</sub>-O<sub>v</sub> and Pd/CeO<sub>2</sub>-OH catalysts exhibit moderate mass activity (MA) of

1,688 and 1,456 mA/mg, respectively, compared with 1,180 mA/mg of Pd/CeO<sub>2</sub>. Particularly, the Pd/CeO<sub>2</sub>·xH<sub>2</sub>O catalyst achieves significantly high mass activity (2,316 mA/mg), which is superior to the commercial Pt/C, Pd/C, and PtRu/C catalysts (Figures S10–S12), and the recently reported Pd/metal oxide, Pd/carbon, and even most Pd-alloy catalysts (Table S1, Supporting Information online). Most importantly, the mass activity of Pd/CeO<sub>2</sub> increases with the content of OH or O<sub>v</sub> (indicated by Ce<sup>3+</sup> fraction) in the ceria support (Figure 3b). Specifically, compared with CeO<sub>2</sub>, CeO<sub>2</sub>-OH has the similar Ce<sup>3+</sup> fraction but higher OH content (9.1% vs. 3.7%). Meanwhile, compared with CeO<sub>2</sub>-OH, CeO<sub>2</sub>-O<sub>v</sub> owns the close OH content but higher Ce<sup>3+</sup> fraction (25.6% vs. 15.7%), and the mass activity of Pd/CeO<sub>2</sub>-O<sub>v</sub> is further enhanced by 16%, confirming the key function of O<sub>v</sub>. When sufficient OH and O<sub>v</sub> simultaneously exist on CeO<sub>2</sub> surface, the catalytic activity of Pd/CeO<sub>2</sub>·xH<sub>2</sub>O can be further improved (Figure 3c). After normalized the mass activities with respect to the corresponding electrochemical active surface areas (ECSA), the specific activities (SA) follow the same trend of Pd/CeO<sub>2</sub>·xH<sub>2</sub>O > Pd/CeO<sub>2</sub>-O<sub>v</sub> > Pd/CeO<sub>2</sub>-OH > Pd/CeO<sub>2</sub> (Table 1). As is well-known, the relative forwarding peak current density (*I<sub>f</sub>*) and backward peak current density (*I<sub>b</sub>*) is generally explored as a standard to estimate the poisoning resistance ability during EOR [41]. The *I<sub>f</sub>*/*I<sub>b</sub>* values of Pd/CeO<sub>2</sub>·xH<sub>2</sub>O, Pd/CeO<sub>2</sub>-O<sub>v</sub>, Pd/CeO<sub>2</sub>-OH, and Pd/CeO<sub>2</sub> are 0.97, 0.65, 0.61, and 0.55, respectively, which indicate that the abundant OH and O<sub>v</sub> can effectively remove the poisonous adsorbates and therefore improve the EOR activity.

Except for the improved electrocatalytic activity of Pd/CeO<sub>2</sub>·xH<sub>2</sub>O catalyst, the stability of the catalyst is also enhanced toward EOR. As depicted in the current-time curves (Figure 3d), the current density of Pd/CeO<sub>2</sub>·xH<sub>2</sub>O catalyst exhibits a slower decay compared with the Pd/CeO<sub>2</sub>-O<sub>v</sub>, Pd/CeO<sub>2</sub>-OH, and Pd/CeO<sub>2</sub> catalyst. After 2,000 s, the remained mass activity of Pd/CeO<sub>2</sub>·xH<sub>2</sub>O catalyst is 499 mA/mg, much higher than those of Pd/CeO<sub>2</sub>-O<sub>v</sub> (285 mA/mg), Pd/CeO<sub>2</sub>-OH (186 mA/mg), and Pd/CeO<sub>2</sub> (80 mA/mg), indicating the higher stability of Pd/CeO<sub>2</sub>·xH<sub>2</sub>O catalyst. Although CeO<sub>2</sub>·xH<sub>2</sub>O promotes the catalytic performance of Pd for EOR, the role of OH and O<sub>v</sub> is still a complex and unresolved problem. Further electrochemical analysis reveals that increasing OH or O<sub>v</sub> on ceria lowers the equilibrium potentials of EOR (Figure 3e), and Pd/CeO<sub>2</sub>·xH<sub>2</sub>O displays the most negative equilibrium potential and thus the fastest reaction kinetics among the four catalysts. Moreover, the electrochemical impedance spectra (Figure S13) imply that Pd/CeO<sub>2</sub>·xH<sub>2</sub>O catalyst possesses the smallest interface charge transfer resistance. Therefore, *via* reducing the interface charge transfer resistance and accelerating the reaction kinetics for EOR, the co-existence of plentiful surface OH and O<sub>v</sub> on CeO<sub>2</sub>·xH<sub>2</sub>O nanoparticles contributes to the

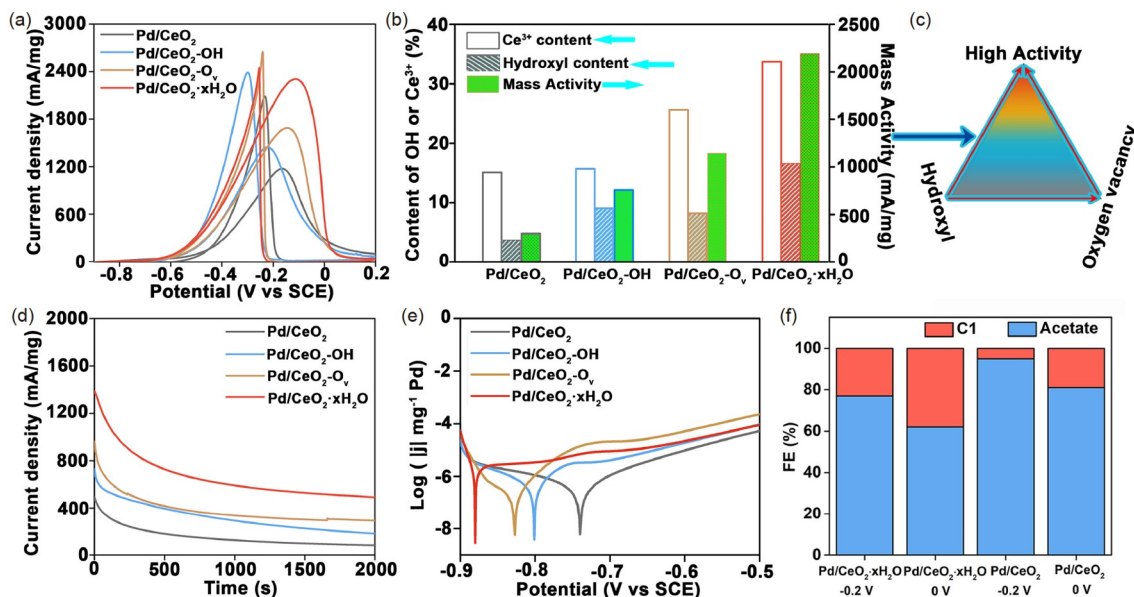


**Figure 3** (a) CV curves of Pd/CeO<sub>2</sub>, Pd/CeO<sub>2</sub>-OH, Pd/CeO<sub>2</sub>-O<sub>v</sub>, and Pd/CeO<sub>2</sub>·xH<sub>2</sub>O in 1.0 M CH<sub>3</sub>CH<sub>2</sub>OH and 1.0 M KOH; (b) effect of hydroxyl or Ce<sup>3+</sup> content in CeO<sub>2</sub> on the mass activity of the catalysts; (c) a volcano plot showing the relation of hydroxyl, oxygen vacancy, and electrocatalytic activity; (d) chronoamperometric curves, and (e) polarization curves of the catalysts; (f) the Faradaic efficiency of each product (C1 and acetate) for the Pd/CeO<sub>2</sub> and Pd/CeO<sub>2</sub>·xH<sub>2</sub>O catalysts at different applied potentials (color online).

**Table 1** Comparison of the EOR performance of the catalysts in alkaline solution

Sample	MA (mA/mg)	ECSA (m <sup>2</sup> /g)	SA (mA/cm <sup>2</sup> )
Pd/CeO <sub>2</sub> ·xH <sub>2</sub> O	2316	31.2	7.4
Pd/CeO <sub>2</sub> -O <sub>v</sub>	1688	28.4	5.9
Pd/CeO <sub>2</sub> -OH	1456	27.2	5.4
Pd/CeO <sub>2</sub>	1180	28.1	4.2

electrocatalytic activity and stability of Pd.

In alkaline media, the rate-determining step of EOR is the removal of CO, the dominant adsorbed species on Pd [42–44]. In order to further investigate the EOR product of the Pd/CeO<sub>2</sub> and Pd/CeO<sub>2</sub>·xH<sub>2</sub>O, we analyzed the liquid phase products (acetate) using high-performance liquid chromatograph (HPLC) after EOR. The Faradaic efficiency for acetate is calculated to be 95% on Pd/CeO<sub>2</sub> at –0.2 V (Figure 3f, Figures S14 and S15), similar to the previous result of Pd/C [15]. The value decreases remarkably to 77% for Pd/CeO<sub>2</sub>·xH<sub>2</sub>O, which indicates that the C1 pathway becomes much more favored on Pd/CeO<sub>2</sub>·xH<sub>2</sub>O compared with Pd/CeO<sub>2</sub>. Therefore, though the C1 pathway is not the dominant route during EOR on Pd catalysts, the strong adsorption ability of CO still makes it as the primary surface poison causing catalyst instability [15]. Next, we investigate the anti-poisoning abilities of the catalysts *via* CO stripping. As shown in Figure 4a, both Pd/CeO<sub>2</sub>-O<sub>v</sub> (–0.231 V) and Pd/CeO<sub>2</sub>-OH (–0.217 V) exhibit more negative onset potential than Pd/CeO<sub>2</sub> (–0.210 V), confirming the function of OH and O<sub>v</sub> in the removal of CO<sub>ads</sub> from the active sites of Pd. Im-

pressively, the Pd/CeO<sub>2</sub>·xH<sub>2</sub>O catalyst with abundant OH and O<sub>v</sub> shows the lowest onset potential of –0.254 V. Meanwhile, compared with the other three catalysts, the larger CO oxidation peak area of Pd/CeO<sub>2</sub>·xH<sub>2</sub>O stands for a larger electrochemical active surface area, which also contributes to the high catalytic performance of Pd/CeO<sub>2</sub>·xH<sub>2</sub>O. As depicted by XPS results (Figure 4b), the Pd 3d binding energies of Pd/CeO<sub>2</sub>-OH, Pd/CeO<sub>2</sub>-O<sub>v</sub>, and Pd/CeO<sub>2</sub>·xH<sub>2</sub>O catalysts all show a positive shift, compared with Pd/CeO<sub>2</sub>, indicating an enhanced electron interaction between Pd and the ceria supports. Furthermore, as evaluated by the surface valence band photoemission spectra (Figure 4c), the d-band

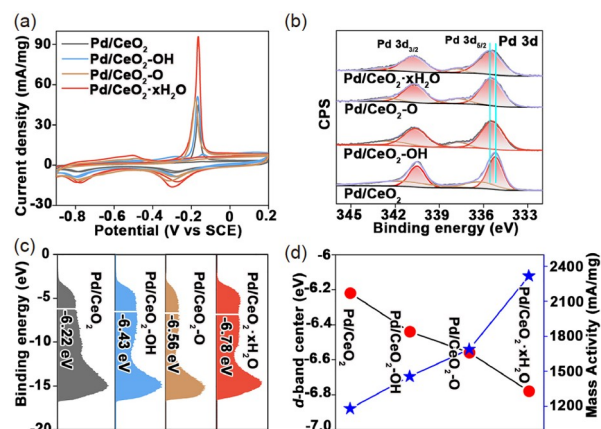


**Figure 4** (a) The CO stripping curves and (b) Pd 3d XPS spectra of the catalysts; (c) the surface valence band photoemission spectra of the catalysts, with the d-band center positions marked by white bars; (d) the mass activity of the catalysts plotted against their d-band center values (red spheres) (color online).

center downshifts in the order of Pd/CeO<sub>2</sub> (−6.22 eV), Pd/CeO<sub>2</sub>-OH (−6.43 eV), Pd/CeO<sub>2</sub>-O<sub>v</sub> (−6.56 eV), and Pd/CeO<sub>2</sub>·xH<sub>2</sub>O (−6.78 eV). The downshift of d-band center can significantly weaken the binding strength of CO on Pd, which results in the improved anti-poisonous ability, and thus further enhances the electrocatalytic activity (Figure 4d) and stability (Figure 3d) [45,46]. These results prove that the ample OH and O<sub>v</sub> on CeO<sub>2</sub>·xH<sub>2</sub>O surface can enhance the interaction between Pd and CeO<sub>2</sub>·xH<sub>2</sub>O, which strongly weakens the adsorption of poisonous intermediates on Pd, leading to the improved activity and stability of Pd/CeO<sub>2</sub>·xH<sub>2</sub>O for EOR.

### 3.3 DFT insight into the mechanism

To further reveal the origin of the superior EOR performance of Pd/CeO<sub>2</sub>·xH<sub>2</sub>O, we conducted the density function theory simulations on Pd/CeO<sub>2</sub>·xH<sub>2</sub>O, Pd/CeO<sub>2</sub>-O<sub>v</sub>, Pd/CeO<sub>2</sub>-OH, and Pd/CeO<sub>2</sub>. We constructed four models of CeO<sub>2</sub>·xH<sub>2</sub>O, CeO<sub>2</sub>-O<sub>v</sub>, CeO<sub>2</sub>-OH, and CeO<sub>2</sub> as the supports, while selected the Pd cluster with six atoms to represent the Pd nanoparticle (Figure S16). It is widely accepted that the adsorption free energy of CO is the crucial factor for describing the EOR activity [25]. As shown in Figure 5a, among the four supported Pd models, Pd/CeO<sub>2</sub>·xH<sub>2</sub>O exhibits the smallest absorption free energy of CO ( $\Delta E = -1.57$  eV), while Pd/CeO<sub>2</sub>-O<sub>v</sub>, Pd/CeO<sub>2</sub>-OH, and Pd/CeO<sub>2</sub> show larger  $\Delta E$  values of −2.04, −2.30, and −2.58 eV, respectively. Figure S17 shows the density of state for the four supported Pd models, from which the d-band centers of Pd/CeO<sub>2</sub>, Pd/CeO<sub>2</sub>-OH, Pd/CeO<sub>2</sub>-O<sub>v</sub>, and Pd/CeO<sub>2</sub>·xH<sub>2</sub>O are calculated to be −2.37, −2.59, −2.84, and −2.97 eV, in line with the decline trend of the experimental results (Figure 4d). Moreover, the downshift of the d-band center is well correlated with the declined  $\Delta E$  values (Figure 5a), which means that the poor match of the d-band with the lowest unoccupied molecular orbital (LUMO) of CO leads to the weakened CO adsorption on Pd (Figure 5b) [47,48].

From the above analysis, we attribute the enhanced EOR performance of Pd/CeO<sub>2</sub>·xH<sub>2</sub>O to the synergy of abundant OH and O<sub>v</sub>. First of all, OH is able to stabilize the O<sub>v</sub> on the surface of CeO<sub>2</sub>·xH<sub>2</sub>O [44]. The sufficient OH and O<sub>v</sub> sy-

nergically modulates the d-band center of Pd, allowing the facilitated removal of poisonous intermediate. Meanwhile, the OH can directly oxidize the intermediate toxic species, such as CO<sub>ads</sub> and CH<sub>ads</sub>, on Pd surface, and the surface O<sub>v</sub> facilitates the adsorption and activation of water to form OH<sub>ads</sub> [33,42,49]. Thus, the coexistence of plentiful OH and O<sub>v</sub> ensures the fast removal of the toxic intermediates for high-efficient EOR.

## 4 Conclusions

In summary, CeO<sub>2</sub> with functional surface, either riched OH or massive O<sub>v</sub>, contributes to the improved catalytic performance of Pd for EOR. CeO<sub>2</sub>·xH<sub>2</sub>O with both abundant OH and O<sub>v</sub> can further enhance the catalytic performance of Pd. We demonstrate that OH and O<sub>v</sub> help to downshift the d-band center of Pd, and alleviate the surface poisoning by CO to improve the catalytic activity. Meanwhile, OH helps to stabilize O<sub>v</sub>, which facilitates the dissociation of water to form OH. Finally, the plentiful OH ensures the efficient removal of toxic intermediates for high catalytic stability. The synergy of OH and O<sub>v</sub> of CeO<sub>2</sub> may find applications in other catalysis system.

**Acknowledgements** This work was supported by the National Natural Science Foundation of China (21875125, 22161033), the 111 Project (D20033), the Natural Science Foundation of Inner Mongolia Autonomous Region of China (2017JQ03), “Grassland Talent” Program and “Grassland Talent” Innovation Team of Inner Mongolia.

**Conflict of interest** The authors declare no conflict of interest.

**Supporting information** The supporting information is available online at <http://chem.scichina.com> and <http://link.springer.com/journal/11426>. The supporting materials are published as submitted, without typesetting or editing. The responsibility for scientific accuracy and content remains entirely with the authors.

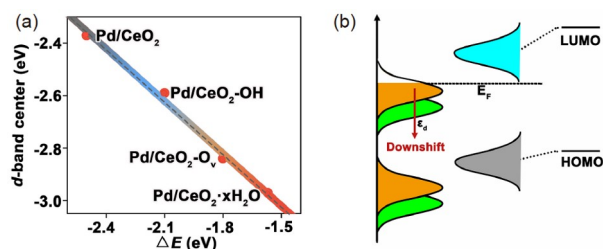


**Figure 5** (a) The calculated values of d-band center and Gibbs free energy of CO on Pd (111) surface; (b) the schematic explanation for the effect of d-band center change on the CO adsorption energy (color online).

- 1 Lv H, Guo X, Sun L, Xu D, Liu B. *Sci China Chem*, 2021, 64: 245–252
- 2 Lv H, Sun L, Zou L, Xu D, Yao H, Liu B. *Chem Sci*, 2019, 10: 1986–1993
- 3 Wang K, Du H, Sripathoorat R, Shen PK. *Adv Mater*, 2018, 30: 1804074
- 4 Wang YF, Zhu C, Yang YY, Zhao ZG. *J Energy Chem*, 2018, 27: 389–394
- 5 Huang W, Kang X, Xu C, Zhou J, Deng J, Li Y, Cheng S. *Adv Mater*, 2018, 30: 1706962
- 6 Xia Z, Guo S. *Chem Soc Rev*, 2019, 48: 3265–3278
- 7 Liu W, Herrmann AK, Geiger D, Borchardt L, Simon F, Kaskel S, Gaponik N, Eychmüller A. *Angew Chem Int Ed*, 2012, 51: 5743–5747
- 8 Chen L, Lu L, Zhu H, Chen Y, Huang Y, Li Y, Wang L. *Nat Commun*, 2017, 8: 14136
- 9 Lyu F, Cao M, Mahsud A, Zhang Q. *J Mater Chem A*, 2020, 8: 15445–15457
- 10 Wang J, Xiao X, Liu Y, Pan K, Pang H, Wei S. *J Mater Chem A*, 2019, 7: 17675–17702

- 11 Wang L, Wu W, Lei Z, Zeng T, Tan Y, Cheng N, Sun X. *J Mater Chem A*, 2020, 8: 592–598
- 12 Xi Z, Erdosy DP, Mendoza-Garcia A, Duchesne PN, Li J, Muzzio M, Li Q, Zhang P, Sun S. *Nano Lett*, 2017, 17: 2727–2731
- 13 Erini N, Beermann V, Gocyla M, Glied M, Heggen M, Dunin-Borkowski RE, Strasser P. *Angew Chem Int Ed*, 2017, 56: 6533–6538
- 14 Zhang S, Liu K, Liu Z, Liu M, Zhang Z, Qiao Z, Ming L, Gao C. *Nano Lett*, 2021, 21: 1074–1082
- 15 Huang W, Ma XY, Wang H, Feng R, Zhou J, Duchesne PN, Zhang P, Chen F, Han N, Zhao F, Zhou J, Cai WB, Li Y. *Adv Mater*, 2017, 29: 1703057
- 16 Jafarian M, Mahjani MG, Heli H, Gopal F, Khajehsharifi H, Hamed MH. *Electrochim Acta*, 2003, 48: 3423–3429
- 17 Zhang J, Ye J, Fan Q, Jiang Y, Zhu Y, Li H, Cao Z, Kuang Q, Cheng J, Zheng J, Xie Z. *J Am Chem Soc*, 2018, 140: 11232–11240
- 18 Yuan Q, Doan HA, Grabow LC, Brankovic SR. *J Am Chem Soc*, 2017, 139: 13676–13679
- 19 Yu K, Ning G, Yang J, Wang Y, Zhang X, Qin Y, Luan C, Yu L, Jiang Y, Luan X, Dong Z, Wang H, Dai X. *J Catal*, 2019, 375: 267–278
- 20 Xie F, Ma L, Gan M, He H, Hu L, Jiang M, Zhang H. *J Power Sources*, 2019, 420: 73–81
- 21 Wu T, Wang X, Emrehan Emre A, Fan J, Min Y, Xu Q, Sun S. *J Energy Chem*, 2021, 55: 48–54
- 22 Shao M, Ning F, Zhao J, Wei M, Evans DG, Duan X. *Adv Funct Mater*, 2013, 23: 3513–3518
- 23 Montini T, Melchionna M, Monai M, Fornasiero P. *Chem Rev*, 2016, 116: 5987–6041
- 24 Qi Z, Chen L, Zhang S, Su J, Somorjai GA. *J Am Chem Soc*, 2021, 143: 60–64
- 25 Tan Q, Shu C, Abbott J, Zhao Q, Liu L, Qu T, Chen Y, Zhu H, Liu Y, Wu G. *ACS Catal*, 2019, 9: 6362–6371
- 26 Ning J, Zhou Y, Shen W. *Sci China Chem*, 2021, 64: 1103–1110
- 27 Li ZY, Zhou J, Tang LS, Fu XP, Wei H, Xue M, Zhao YL, Jia CJ, Li XM, Chu HB, Li Y. *J Mater Chem A*, 2018, 6: 2318–2326
- 28 Cai Z, Bi Y, Hu E, Liu W, Dwarica N, Tian Y, Li X, Kuang Y, Li Y, Yang X-, Wang H, Sun X. *Adv Energy Mater*, 2018, 8: 1701694
- 29 Liu B, Liu J, Li T, Zhao Z, Gong XQ, Chen Y, Duan A, Jiang G, Wei Y. *J Phys Chem C*, 2015, 119: 12923–12934
- 30 Bligaard T, Nørskov JK. *Electrochim Acta*, 2007, 52: 5512–5516
- 31 Chen B, Ma Y, Ding L, Xu L, Wu Z, Yuan Q, Huang W. *J Phys Chem C*, 2013, 117: 5800–5810
- 32 Song YL, Yin LL, Zhang J, Hu P, Gong XQ, Lu G. *Surf Sci*, 2013, 618: 140–147
- 33 Wu XP, Gong XQ. *Phys Rev Lett*, 2016, 116: 086102
- 34 Fronzi M, Piccinin S, Delley B, Traversa E, Stampfl C. *Phys Chem Chem Phys*, 2009, 11: 9188–9199
- 35 Abi-aad E, Bechara R, Grimblot J, Aboukais A. *Chem Mater*, 1993, 5: 793–797
- 36 Tao L, Shi Y, Huang YC, Chen R, Zhang Y, Huo J, Zou Y, Yu G, Luo J, Dong CL, Wang S. *Nano Energy*, 2018, 53: 604–612
- 37 Wang T, Sun DC. *Mater Res Bull*, 2008, 43: 1754–1760
- 38 Lin B, Fang B, Wu Y, Li C, Ni J, Wang X, Lin J, Au C, Jiang L. *ACS Catal*, 2021, 11: 1331–1339
- 39 Jiang S, Zhang R, Liu H, Rao Y, Yu Y, Chen S, Yue Q, Zhang Y, Kang Y. *J Am Chem Soc*, 2020, 142: 6461–6466
- 40 Liang X, Wang P, Gao Y, Huang H, Tong F, Zhang Q, Wang Z, Liu Y, Zheng Z, Dai Y, Huang B. *Appl Catal B-Environ*, 2020, 260: 118151
- 41 Liu J, Luo Z, Li J, Yu X, Llorca J, Nasidou D, Arbiol J, Meyns M, Cabot A. *Appl Catal B-Environ*, 2019, 242: 258–266
- 42 Wang Y, Zou S, Cai WB. *Catalysts*, 2015, 5: 1507–1534
- 43 Wang F, Yu H, Tian Z, Xue H, Feng L. *J Energy Chem*, 2018, 27: 395–403
- 44 Li M, Zhao Z, Zhang W, Luo M, Tao L, Sun Y, Xia Z, Chao Y, Yin K, Zhang Q, Gu L, Yang W, Yu Y, Lu G, Guo S. *Adv Mater*, 2021, 33: 2103762
- 45 Li Z, Ai X, Chen H, Liang X, Li X, Wang D, Zou X. *Chem Commun*, 2021, 57: 5075–5078
- 46 Li Z, Li J, Jiang K, Yuan S, Yu D, Wei H, Shi Z, Li X, Chu H. *Chem Eng J*, 2021, 411: 128527
- 47 Hu S, Munoz F, Noborikawa J, Haan J, Scudiero L, Ha S. *Appl Catal B-Environ*, 2016, 180: 758–765
- 48 Li Z, Xie Z, Chen H, Liang X, Ai X, Yuan L, Li X, Zou X. *Chem Eng J*, 2021, 419: 129568
- 49 Zhang X, Zhou D, Wang X, Zhou J, Li J, Zhang M, Shen Y, Chu H, Qu Y. *ACS Catal*, 2020, 10: 3832–3837